Further Investigation of Modeling Limit Cycle Oscillation Behavior of the F-16 Fighter Using a Harmonic Balance Approach

Jeffrey P. Thomas, * Earl H. Dowell, † Kenneth C. Hall ‡
Duke University, Durham, NC 27708–0300

and

Charles M. Denegri Jr. §
U.S. Air Force SEEK EAGLE Office, Eglin Air Force Base, Florida 32542-6865

A computational investigation of limit cycle oscillation behavior of the F-16 fighter configuration using a nonlinear frequency-domain harmonic-balance approach is presented. The research discussed in this latest paper is a follow-on to our work presented at the 2004 SDM conference. Our latest efforts have been directed toward assessing the effects of mean angle-of-attack, wingtip geometry, wing twist, and static aeroelastic deformation on flutter onset and LCO response.

Introduction

Our latest efforts are a follow-on to the research efforts reported in Thomas, Dowell and Hall[1] where the harmonic balance (HB) technique for modeling nonlinear unsteady aerodynamics (see Hall et al.[2] and Thomas, Dowell, and Hall[3–6]) is used to determine the limit cycle oscillation (LCO) behavior of the F-16 fighter aircraft.

In the following, we now consider the influence of angle-of-attack, wingtip geometry, wing twist, and the modeling of static aeroelastic effects on flutter onset and LCO response. We are finding that flutter onset and especially the subsequent LCO behavior are very sensitive to these parameters. In Thomas, Dowell, and Hall,[1] we considered the wing mean shape to be the jig shape. We also chose the steady flow angle-of-attack to be a constant value of 1.5 degrees. We find that flutter onset is not very sensitive to the number of structural modes used so long as at least the first two antisymmetric mode shapes are used in the structural portion of the aeroelastic model.

Flutter onset and LCO response behavior of the F-16 fighter is in general dependent on the specific exteral stores being carried by the airplane as well as the Mach number and altitude at which the aircraft is being flown. In the following, we will demostrate how a novel nonlinear frequency domain harmonic technique can be used to rapidly determine the flutter onset Mach number for a specified altitude along with the subsequent finite amplitude LCO dynamic response of the aircraft when the F-16 is flown further into the unstable region beyond the altitude versus Mach number flutter boundary.

The flow solver portion of the aeroelastic model consists of a high fidelity nonlinear unsteady frequency domain compressible Reynolds averaged Navier Stokes (RANS) solver for the F-16 wing aerodynamic pressures. The structural portion consists of a linear modal based model using mode shapes and modal masses obtained from a NASTRAN finite element model of the entire airplane configuration including fuselage, horizontal tail, and external weapons and stores. The structural damping to taken to be zero.

In the present analysis, we study sensitivities of the computed flutter onset and LCO response to parameters such as mean angle-of-attack, wing tip geometry, wing twist, and static aeroelastic wing deformation effects. At the present time, we are not to a level of computational sophistication in our fluid dynamic model to be able to model aerodynamically the complete F-16 aircraft, i.e. the wing, fuselage, horizontal tail, vertical tail, weapons and external stores, control surfaces, etc. Our goals at present are to gain insight into the sensensitives of computed flutter onset and LCO behavior to the structural and aerodynamic details of the computational model.

*Research Assistant Professor, Department of Mechanical Engineering and Materials Science, Senior Member AIAA.

†J. A. Jones Professor, Department of Mechanical Engineering and Materials Science, and Dean Emeritus, School of Engineering, Fellow AIAA.

‡Professor and Department Chairperson, Department of Mechanical Engineering and Materials Science, Associate Fellow AIAA.

§Lead Flutter Engineer, Engineering Division, Certification Division, 205 West D Avenue, Suite 348. Senior Member AIAA.

Copyright © 2005 by Jeffrey P. Thomas, Earl H. Dowell, Kenneth C. Hall and Charles M. Denegri Jr.. Published by the American Institute of Aeronautics and Astronautics, Inc. with permission.

Theory

Aeroelasitc Model Governing Equations

We consider a structural modal based aeroelastic model. In this case, the structural model is linear with no structural damping, although damping can also be easily incorporated. The governing aeroelastic equation can be written in the time-domain as:

$$\mathbf{R}(t) = \boldsymbol{\mathcal{M}}\left(\mathbf{I}\frac{d^2\boldsymbol{\xi}}{dt} + \boldsymbol{\Omega}^2\boldsymbol{\xi}\right) - q_\infty S\boldsymbol{C}_{\boldsymbol{\mathcal{Q}}} + g\mathbf{f}_{\boldsymbol{\phi}_m} = \mathbf{0} \quad (1)$$

where $\mathbf{R}(t)$ is a M dimensional vector (M being the number of structural modes used in the model) representing the residual of this equation, $\boldsymbol{\mathcal{M}}$ is a matrix with the model structural modal masses on the diagonal, $\boldsymbol{\Omega}$ is matrix with the model structural modal frequencies on the diagonal, $\boldsymbol{\xi}$ is the M dimensional vector of structural modal coordinates, q_∞ is the freestream dynamic pressure, S is the configuration reference area, $\boldsymbol{C}_{\boldsymbol{\mathcal{Q}}}$ is the M dimensional vector of modal forces, and $g\mathbf{f}_{\boldsymbol{\phi}_m}$ is the M dimensional vector of modal forces due to gravitational effects.

We can also consider the airplane six degree-of-freedom static rigid body trim conditions in the overall analysis, however we will not be doing this in the present paper. One reason for this is that at the current stage of development of our computational model, we are not yet aerodynamically modeling the F-16 elevator. As such we cannot solve for a trimmed aircraft pitch condition. So in the following, the analysis will be based on a prescribed mean aircraft angle-of-attack α_0.

Next, we consider the structural motion $\boldsymbol{\xi}$ and the modal loading $\boldsymbol{C}_{\boldsymbol{\mathcal{Q}}}$ to be periodic in time. i.e.

$$\boldsymbol{\xi}(t) = \hat{\boldsymbol{\xi}}_0 + \sum_{n=1}^{\infty}\left(\hat{\boldsymbol{\xi}}_{c_n}\cos(\omega n t) + \hat{\boldsymbol{\xi}}_{s_n}\sin(\omega n t)\right) \quad (2)$$

and

$$\boldsymbol{C}_{\boldsymbol{\mathcal{Q}}}(t) = \hat{\boldsymbol{C}}_{\boldsymbol{\mathcal{Q}}0} + \sum_{n=1}^{\infty}\left(\hat{\boldsymbol{C}}_{\boldsymbol{\mathcal{Q}}c_n}\cos(\omega n t) + \hat{\boldsymbol{C}}_{\boldsymbol{\mathcal{Q}}s_n}\sin(\omega n t)\right). \quad (3)$$

As such, Eq. 1 can be written as

$$\mathbf{R}(t) = \hat{\mathbf{R}}_0 + \sum_{n=1}^{\infty}\left(\hat{\mathbf{R}}_{c_n}\cos(\omega n t) + \hat{\mathbf{R}}_{s_n}\sin(\omega n t)\right) \quad (4)$$

or

$$\begin{aligned}&\mathbf{R}(t) = \\ &\boldsymbol{\mathcal{M}}\boldsymbol{\Omega}^2\hat{\boldsymbol{\xi}}_0 - q_\infty S\hat{\boldsymbol{C}}_{\boldsymbol{\mathcal{Q}}0} + g\mathbf{f}_{\boldsymbol{\phi}_m} + \\ &\sum_{n=1}^{\infty}\left[\boldsymbol{\mathcal{M}}(-n^2\omega^2\mathbf{I} + \boldsymbol{\Omega}^2)\hat{\boldsymbol{\xi}}_{c_n} - q_\infty S\hat{\boldsymbol{C}}_{\boldsymbol{\mathcal{Q}}c_n}\right]\cos(\omega n t) + \\ &\sum_{n=1}^{\infty}\left[\boldsymbol{\mathcal{M}}(-n^2\omega^2\mathbf{I} + \boldsymbol{\Omega}^2)\hat{\boldsymbol{\xi}}_{s_n} - q_\infty S\hat{\boldsymbol{C}}_{\boldsymbol{\mathcal{Q}}s_n}\right]\sin(\omega n t) = \mathbf{0}.\end{aligned} \quad (5)$$

We can then do an inverse Fourier transformation to determine the Fourier coefficients $\hat{\mathbf{R}}_0$, $\hat{\mathbf{R}}_{c_n}$, $\hat{\mathbf{R}}_{s_n}$. i.e.

$$\begin{aligned}\hat{\mathbf{R}}_0 &= \frac{\omega}{2\pi}\int_0^{2\pi/\omega}\mathbf{R}(t)\,\mathrm{dt}, \\ \hat{\mathbf{R}}_{c_n} &= \frac{\omega}{\pi}\int_0^{2\pi/\omega}\mathbf{R}(t)\cos(\omega n t)\,\mathrm{dt}, \\ \hat{\mathbf{R}}_{s_n} &= \frac{\omega}{\pi}\int_0^{2\pi/\omega}\mathbf{R}(t)\sin(\omega n t)\,\mathrm{dt}.\end{aligned} \quad (6)$$

This yields

$$\begin{aligned}\hat{\mathbf{R}}_0 &= \boldsymbol{\mathcal{M}}\boldsymbol{\Omega}^2\hat{\boldsymbol{\xi}}_0 - q_\infty S\hat{\boldsymbol{C}}_{\boldsymbol{\mathcal{Q}}0} + g\mathbf{f}_{\boldsymbol{\phi}_m}, \\ \hat{\mathbf{R}}_{c_n} &= \boldsymbol{\mathcal{M}}(-n^2\omega^2\mathbf{I} + \boldsymbol{\Omega}^2)\hat{\boldsymbol{\xi}}_{c_n} - q_\infty S\hat{\boldsymbol{C}}_{\boldsymbol{\mathcal{Q}}c_n}, \\ \hat{\mathbf{R}}_{s_n} &= \boldsymbol{\mathcal{M}}(-n^2\omega^2\mathbf{I} + \boldsymbol{\Omega}^2)\hat{\boldsymbol{\xi}}_{s_n} - q_\infty S\hat{\boldsymbol{C}}_{\boldsymbol{\mathcal{Q}}s_n}.\end{aligned} \quad (7)$$

In order to satisfy $\mathbf{R}(t) = \mathbf{0}$, $\hat{\mathbf{R}}_0$, $\hat{\mathbf{R}}_{c_n}$, and $\hat{\mathbf{R}}_{s_n}$ (for all n) must be equal to zero. i.e.

$$\begin{aligned}\boldsymbol{\mathcal{M}}\boldsymbol{\Omega}^2\hat{\boldsymbol{\xi}}_0 - q_\infty S\hat{\boldsymbol{C}}_{\boldsymbol{\mathcal{Q}}0} + g\mathbf{f}_{\boldsymbol{\phi}_m} &= \mathbf{0}, \\ \boldsymbol{\mathcal{M}}(-n^2\omega^2\mathbf{I} + \boldsymbol{\Omega}^2)\hat{\boldsymbol{\xi}}_{c_n} - q_\infty S\hat{\boldsymbol{C}}_{\boldsymbol{\mathcal{Q}}c_n} &= \mathbf{0}, \\ \boldsymbol{\mathcal{M}}(-n^2\omega^2\mathbf{I} + \boldsymbol{\Omega}^2)\hat{\boldsymbol{\xi}}_{s_n} - q_\infty S\hat{\boldsymbol{C}}_{\boldsymbol{\mathcal{Q}}s_n} &= \mathbf{0}\end{aligned} \quad (8)$$

for all n.

Simplification of Aeroelastic Governing Equations

In the following, we consider the structural dynamic motion $\boldsymbol{\xi}$ to be strictly harmonic. i.e.

$$\boldsymbol{\xi} = \hat{\boldsymbol{\xi}}_0 + \hat{\boldsymbol{\xi}}_{c_1}\cos(\omega t) + \hat{\boldsymbol{\xi}}_{s_1}\sin(\omega t). \quad (9)$$

However, the aerodynamic loading will still be considered to consist of higher harmonic components as per Eq. 3. We also consider the motion of the first structural modal coordinate to be of the form

$$\xi_1(t) = \hat{\xi}_{1_0} + \hat{\xi}_{1_{c_1}}\cos(\omega t), \quad (10)$$

and we define an alternate set of unsteady modal coordinates ($\hat{\boldsymbol{\xi}}'_{c_1}$ and $\hat{\boldsymbol{\xi}}'_{s_1}$)

$$\hat{\boldsymbol{\xi}}'_{c_1} = \begin{Bmatrix} 1 \\ \hat{\xi}_{2_{c_1}}/\hat{\xi}_{1_{c_1}} \\ \vdots \\ \hat{\xi}_{M_{c_1}}/\hat{\xi}_{1_{c_1}} \end{Bmatrix} \qquad \hat{\boldsymbol{\xi}}'_{s_1} = \begin{Bmatrix} 0 \\ \hat{\xi}_{2_{s_1}}/\hat{\xi}_{1_{c_1}} \\ \vdots \\ \hat{\xi}_{M_{s_1}}/\hat{\xi}_{1_{c_1}} \end{Bmatrix} \quad (11)$$

so that $\boldsymbol{\xi}$ can also be expressed as

$$\boldsymbol{\xi} = \hat{\boldsymbol{\xi}}_0 + \hat{\xi}_{1_{c_1}}\left(\hat{\boldsymbol{\xi}}'_{c_1}\cos(\omega t) + \hat{\boldsymbol{\xi}}'_{s_1}\sin(\omega t)\right). \quad (12)$$

Note, the dynamic pressure q_∞ can be expressed as a function of flight altitude h and Mach number M_∞, i.e.

$$q_\infty = \frac{\gamma}{2}M_\infty^2 p_\infty(h). \quad (13)$$

The notation $p_\infty(h)$ is to signify that freestream static pressure p_∞ is a function of flight altitude h when considering standard atmospheric conditions.

By assuming harmonic motion, and substituting the altitude and Mach number relation for dynamic pressure, the governing frequency domain aeroelastic equations (Eq. 8) become

$$\begin{aligned}\boldsymbol{\mathcal{M}}\boldsymbol{\Omega}^2\hat{\boldsymbol{\xi}}_0 - \frac{\gamma}{2}M_\infty^2 p_\infty(h)S\hat{\boldsymbol{C}}_{\boldsymbol{\mathcal{Q}}0} - g\mathbf{f}_{\boldsymbol{\phi}m} &= \mathbf{0},\\ \hat{\xi}_{1_{c_1}}\boldsymbol{\mathcal{M}}(\omega^2\mathbf{I}+\boldsymbol{\Omega}^2)\hat{\boldsymbol{\xi}}_{c_1}^{'} - \frac{\gamma}{2}M_\infty^2 p_\infty(h)S\hat{\boldsymbol{C}}_{\boldsymbol{\mathcal{Q}}c_1} &= \mathbf{0},\\ \hat{\xi}_{1_{c_1}}\boldsymbol{\mathcal{M}}(\omega^2\mathbf{I}+\boldsymbol{\Omega}^2)\hat{\boldsymbol{\xi}}_{s_1}^{'} - \frac{\gamma}{2}M_\infty^2 p_\infty(h)S\hat{\boldsymbol{C}}_{\boldsymbol{\mathcal{Q}}s_1} &= \mathbf{0}.\end{aligned} \tag{14}$$

The harmonic balance computational fluid dynamic method described subsequently will be used to compute the harmonic modal forces $\hat{\boldsymbol{C}}_{\boldsymbol{\mathcal{Q}}0}$ $\hat{\boldsymbol{C}}_{\boldsymbol{\mathcal{Q}}c_1}$, and $\hat{\boldsymbol{C}}_{\boldsymbol{\mathcal{Q}}s_1}$. These quantities are a function of the freestream Mach number M_∞, flight altitude h, frequency ω, and the modal motion coordinates $\boldsymbol{\xi}$. i.e.

$$\begin{aligned}\hat{\boldsymbol{C}}_{\boldsymbol{\mathcal{Q}}0} &= \hat{\boldsymbol{C}}_{\boldsymbol{\mathcal{Q}}0}(\alpha_0, M_\infty, h, \hat{\xi}_{1_{c_1}}, \omega, \hat{\boldsymbol{\xi}}_0, \hat{\boldsymbol{\xi}}_{c_1}^{'}, \hat{\boldsymbol{\xi}}_{s_1}^{'}),\\ \hat{\boldsymbol{C}}_{\boldsymbol{\mathcal{Q}}c_1} &= \hat{\boldsymbol{C}}_{\boldsymbol{\mathcal{Q}}c_1}(\alpha_0, M_\infty, h, \hat{\xi}_{1_{c_1}}, \omega, \hat{\boldsymbol{\xi}}_0, \hat{\boldsymbol{\xi}}_{c_1}^{'}, \hat{\boldsymbol{\xi}}_{s_1}^{'}),\\ \hat{\boldsymbol{C}}_{\boldsymbol{\mathcal{Q}}s_1} &= \hat{\boldsymbol{C}}_{\boldsymbol{\mathcal{Q}}s_1}(\alpha_0, M_\infty, h, \hat{\xi}_{1_{c_1}}, \omega, \hat{\boldsymbol{\xi}}_0, \hat{\boldsymbol{\xi}}_{c_1}^{'}, \hat{\boldsymbol{\xi}}_{s_1}^{'}).\end{aligned} \tag{15}$$

For a fixed angle of attack α_0, if one specifies Mach number M_∞ and altitude h, Eq. 14 constitutes a system of $3 \times M$ equations for the unknowns of first structural modal coordinate unsteady first harmonic amplitude $\hat{\xi}_{1_{c_1}}$, frequency ω, the M unknown zeroth harmonic structural modal coordinates $\hat{\boldsymbol{\xi}}_0$, and the $2 \times (M-1)$ first harmonic structural modal coordinates of $\hat{\boldsymbol{\xi}}_{c_1}^{'}$ and $\hat{\boldsymbol{\xi}}_{s_1}^{'}$. i.e. a total of $3 \times M$ unknowns. Similarly, for a fixed angle of attack α_0, if one instead specifies the first structural modal coordinate unsteady first harmonic amplitude $\hat{\xi}_{1_{c_1}}$ and the altitude h, then Eq. 14, represents a system of $3 \times M$ for the unknowns of Mach number M_∞, frequency ω, the M unknown zeroth harmonic structural modal coordinates $\hat{\boldsymbol{\xi}}_0$, and the $2 \times (M-1)$ first harmonic structural modal coordinates of $\hat{\boldsymbol{\xi}}_{c_1}^{'}$ and $\hat{\boldsymbol{\xi}}_{s_1}^{'}$.

We prefer to take the latter approach in solving the system of aeroelastic equations since this enables us to solve for the flutter onset condition directly. To solve for the flutter onset condition we simply specify a very small amplitude of the first structural modal coordinate unsteady first harmonic amplitude $\hat{\xi}_{1_{c_1}}$. Then for LCO conditions deeper into the unstable aeroelastic region, we simply specify ever increasing values for the first structural modal coordinate unsteady first harmonic amplitude $\hat{\xi}_{1_{c_1}}$.

Aeroelastic Solution Process

Consider the system of Eq. 14 written in vector form as

$$\mathbf{R}(\mathbf{L}) = \mathbf{0} \tag{16}$$

where

$$\mathbf{R}(\mathbf{L}) = \left\{\begin{array}{c} \boldsymbol{\mathcal{M}}\boldsymbol{\Omega}^2\hat{\boldsymbol{\xi}}_0 - \frac{1}{2}\gamma M_\infty^2 f(h)S\hat{\boldsymbol{C}}_{\boldsymbol{\mathcal{Q}}0} - g\mathbf{f}_{\boldsymbol{\phi}m} \\ \hat{\xi}_{1_{c_1}}\boldsymbol{\mathcal{M}}(\omega^2\mathbf{I}+\boldsymbol{\Omega}^2)\hat{\boldsymbol{\xi}}_{c_1}^{'} - \frac{\gamma}{2}M_\infty^2 p_\infty(h)S\hat{\boldsymbol{C}}_{\boldsymbol{\mathcal{Q}}c_1} \\ \hat{\xi}_{1_{c_1}}\boldsymbol{\mathcal{M}}(\omega^2\mathbf{I}+\boldsymbol{\Omega}^2)\hat{\boldsymbol{\xi}}_{s_1}^{'} - \frac{\gamma}{2}M_\infty^2 p_\infty(h)S\hat{\boldsymbol{C}}_{\boldsymbol{\mathcal{Q}}s_1} \end{array}\right\} \tag{17}$$

and

$$\mathbf{L} = \left\{\begin{array}{c} M_\infty \\ \omega \\ \hat{\xi}_{1_0} \\ \vdots \\ \hat{\xi}_{M_0} \\ \hat{\xi}_{2_{c_1}}/\hat{\xi}_{1_{c_1}} \\ \vdots \\ \hat{\xi}_{M_{c_1}}/\hat{\xi}_{1_{c_1}} \\ \hat{\xi}_{2_{s_1}}/\hat{\xi}_{1_{c_1}} \\ \vdots \\ \hat{\xi}_{M_{s_1}}/\hat{\xi}_{1_{c_1}} \end{array}\right\}. \tag{18}$$

We have found that an efficient method for solving Eq. 16 is to use the Newton-Raphson root finding technique. This provides an iterative method for solving for the unknown LCO variables $\mathbf{L}$ whereby one iteratively marches the vector equation

$$\mathbf{L}^{n+1} = \mathbf{L}^n - \left[\frac{\partial \mathbf{R}(\mathbf{L}^n)}{\partial \mathbf{L}}\right]^{-1}\mathbf{R}(\mathbf{L}^n) \tag{19}$$

until a suitable level of convergence is achieved.

We have also observed that one can use simple forward finite-differences to compute the column vectors of $\partial\mathbf{R}(\mathbf{L})/\partial\mathbf{L}$. That is,

$$\left[\frac{\partial \mathbf{R}(\mathbf{L})}{\partial \mathbf{L}}\right] = \left[\begin{array}{cccc} | & | & | & | \\ \frac{\partial \mathbf{R}}{\partial M_\infty} & \frac{\partial \mathbf{R}}{\partial \omega} & \cdots & \frac{\partial \mathbf{R}}{\partial(\hat{\xi}_{M_{s_1}}/\hat{\xi}_{1_{c_1}})} \\ | & | & | & | \end{array}\right] \tag{20}$$

where for example

$$\frac{\partial \mathbf{R}(\mathbf{L})}{\partial M_\infty} \approx \frac{\mathbf{R}(\mathbf{L}, M_\infty + \epsilon) - \mathbf{R}(\mathbf{L}, M_\infty)}{\epsilon},$$

$$\frac{\partial \mathbf{R}(\mathbf{L})}{\partial \omega} \approx \frac{\mathbf{R}(\mathbf{L}, \omega + \epsilon) - \mathbf{R}(\mathbf{L}, \omega)}{\epsilon},$$

etc. for a small ϵ. Determining the column vectors of $\partial\mathbf{R}/\partial\mathbf{L}$ in this manner thus requires numerous computations of $\mathbf{R}(\mathbf{L})$ for various perturbations to $\mathbf{L}$. This in turn means several computations of the unsteady aerodynamic loading $\boldsymbol{\mathcal{C}}_{\boldsymbol{\mathcal{Q}}}$ for the different perturbations of $\mathbf{L}$, and this is where the harmonic balance solver is utilized.

One further simplification to solving Eq. 16 is that the static aeroelastic deformation components $\hat{\boldsymbol{\xi}}_0$ may be expressed as

$$\hat{\boldsymbol{\xi}}_0 = \left(\boldsymbol{\mathcal{M}}\boldsymbol{\Omega}^2\right)^{-1}\left(\frac{\gamma}{2}M_\infty^2 p_\infty(h) S\hat{\boldsymbol{C}}_{\boldsymbol{\mathcal{Q}}0} + g\mathbf{f}_{\boldsymbol{\phi}m}\right) \quad (21)$$

So in an iterative fashion, one can determine explicitly an update for $\hat{\boldsymbol{\xi}}_0$ using the following equation

$$\hat{\boldsymbol{\xi}}_0^{n+1} = \left(\boldsymbol{\mathcal{M}}\boldsymbol{\Omega}^2\right)^{-1}\left(\frac{\gamma}{2}M_\infty^2 p_\infty(h) S\hat{\boldsymbol{C}}_{\boldsymbol{\mathcal{Q}}0}{}^{n} + g\mathbf{f}_{\boldsymbol{\phi}m}\right) \quad (22)$$

where $\hat{\boldsymbol{\xi}}_0^{n+1}$ is the update to static model coordinates at the n^{th} iteration, and $\hat{\boldsymbol{C}}_{\boldsymbol{\mathcal{Q}}0}{}^{n}$ is the static modal forces based on the static model coordinates at the n^{th} iteration. i.e. $\hat{\boldsymbol{\xi}}_0^{n}$.

The Harmonic Balance Method

The harmonic balance (HB) computational fluid dynamic (CFD) method development proceeds by first considering the chosen CFD method as representing a solver for a large system of ordinary differential equations (ODE's), which may be expressed as

$$R_{l,j}(t) = \frac{dQ_{l,j}(t)}{dt} - N_{l,j}(t) = 0 \quad (23)$$

where the subscript j represents a specific mesh point in the discrete computational spatial domain, and the subscript l represents a specific dependent variable at mesh point j. As such, $Q_{l,j}$ denotes the l^{th} CFD solution independent variable at mesh point j, and $N_{l,j}$ denotes l^{th} component of the CFD solver residual at mesh point j.

The next step in HB/CFD method development is that we consider the CFD solution $Q_{l,j}$ and CFD residual $N_{l,j}$ to be periodic in time and of a fundamental frequency ω. This enables us to expand the CFD solution and residual in a Fourier series as

$$Q_{l,j}(t) = \hat{Q}_{l,j_0} + \sum_{n=1}^{\infty}\left(\hat{Q}_{l,j_{c_n}}\cos(\omega nt) + \hat{Q}_{l,j_{s_n}}\sin(\omega nt)\right) \quad (24)$$

$$N_{l,j}(t) = \hat{N}_{l,j_0} + \sum_{n=1}^{\infty}\left(\hat{N}_{l,j_{c_n}}\cos(\omega nt) + \hat{N}_{l,j_{s_n}}\sin(\omega nt)\right). \quad (25)$$

We next assume the CFD solution and residual can still be accurately represented if these Fourier expansions are truncated to a specified and sufficient number of harmonics N_H. i.e.

$$Q_{l,j}(t) \approx \hat{Q}_{l,j_0} + \sum_{n=1}^{N_H}\left(\hat{Q}_{l,j_{c_n}}\cos(\omega nt) + \hat{Q}_{l,j_{s_n}}\sin(\omega nt)\right) \quad (26)$$

$$N_{l,j}(t) \approx \hat{N}_{l,j_0} + \sum_{n=1}^{N_H}\left(\hat{N}_{l,j_{c_n}}\cos(\omega nt) + \hat{N}_{l,j_{s_n}}\sin(\omega nt)\right). \quad (27)$$

The next step of the HB/CFD method development consists of substituting these expansion into Eq. 23, which allows Eq. 23 to also be considered as a truncated Fourier expansion. i.e

$$R_{l,j}(t) \approx \hat{R}_{l,j_0} + \sum_{n=1}^{N_H}\left(\hat{R}_{l,j_{c_n}}\cos(\omega nt) + \hat{R}_{l,j_{s_n}}\sin(\omega nt)\right). \quad (28)$$

We then Fourier transform Eq. 28 in order to determine the Fourier harmonic component terms $\hat{R}_{l,j_0}$, $\hat{R}_{l,j_{c_n}}$ and $\hat{R}_{l,j_{s_n}}$. i.e.

$$\begin{aligned}
\hat{R}_{l,j_0} &= \frac{\omega}{2\pi}\int_0^{2\pi/\omega} R_{l,j}(t)\mathrm{d}t = \hat{N}_{l,j_0},\\
\hat{R}_{l,j_{c_n}} &= \frac{\omega}{\pi}\int_0^{2\pi/\omega} R_{l,j}(t)\cos(\omega nt)\mathrm{d}t = \omega n\hat{Q}_{l,j_{s_n}} + \hat{N}_{l,j_{c_n}},\\
\hat{R}_{l,j_{s_n}} &= \frac{\omega}{\pi}\int_0^{2\pi/\omega} R_{l,j}(t)\sin(\omega nt)\mathrm{d}t = -\omega n\hat{Q}_{l,j_{c_n}} + \hat{N}_{l,j_{s_n}}.
\end{aligned} \quad (29)$$

$R_{l,j}(t) = 0$ implies that $\hat{R}_{l,j_0} = 0$, $\hat{R}_{l,j_{c_n}} = 0$ and $\hat{R}_{l,j_{s_n}} = 0$ so that

$$\begin{aligned}
\hat{N}_{l,j_0} &= 0\\
\omega n\hat{Q}_{l,j_{s_n}} + \hat{N}_{l,j_{c_n}} &= 0\\
-\omega n\hat{Q}_{l,j_{c_n}} + \hat{N}_{l,j_{s_n}} &= 0
\end{aligned} \quad (30)$$

for $n = 1, 2, \ldots, N_H$. This constitutes a system of N_T where

$$N_T = 2N_H + 1 \quad (31)$$

equations for the N_T unknown Fourier harmonic terms $\hat{Q}_{l,j_0}$, $\hat{Q}_{l,j_{s_n}}$, and $\hat{Q}_{l,j_{c_n}}$ $(n = 1, 2, \ldots, N_H)$ that can also be written in vector and matrix form as

$$\omega\mathbf{A}\hat{\boldsymbol{\mathcal{Q}}}_{l,j} + \hat{\boldsymbol{\mathcal{N}}}_{l,j} = \hat{\mathbf{0}} \quad (32)$$

where

$$\hat{\boldsymbol{\mathcal{Q}}}_{l,j} = \begin{Bmatrix} \hat{Q}_{l,j_0}\\ \hat{Q}_{l,j_{c_1}}\\ \vdots\\ \hat{Q}_{l,j_{c_{N_H}}}\\ \hat{Q}_{l,j_{c_1}}\\ \vdots\\ \hat{Q}_{l,j_{s_{N_H}}} \end{Bmatrix}, \quad \hat{\boldsymbol{\mathcal{N}}}_{l,j} = \begin{Bmatrix} \hat{N}_{l,j_0}\\ \hat{N}_{l,j_{c_1}}\\ \vdots\\ \hat{N}_{l,j_{c_{N_H}}}\\ \hat{N}_{l,j_{c_1}}\\ \vdots\\ \hat{N}_{l,j_{s_{N_H}}} \end{Bmatrix}, \quad (33)$$

and $\mathbf{A}$ is $N_T \times N_T$ matrix with row/column entries $A_{i,j}$ given by $A_{i=n+1,j=N_H+1+n} = n$ and $A_{i=n+1,j=N_H+1+n} = -n$ for $n = 1, 2, \ldots, N_H$, and all other elements of $\mathbf{A}$ being equal to zero. i.e.

$$\mathbf{A} = \begin{bmatrix} 0 & & & & & & \\ & & & 1 & & & \\ & & & & \ddots & & \\ & & & & & & N_H \\ & -1 & & & & & \\ & & \ddots & & & & \\ & & & -N_H & & & \end{bmatrix} \quad (34)$$

Although one could write a flow solver based on Eq. 32, depending on degree of nonlinearity of the CFD solver, the Fourier residual terms of $\hat{\boldsymbol{\mathcal{N}}}_{l,j}$ may be very complex functions of the Fourier solution variables $\hat{\boldsymbol{\mathcal{Q}}}_{l,j}$. It may in fact be very difficult if not impossible to determine explicit expressions for the terms of $\hat{\boldsymbol{\mathcal{N}}}_{l,j}$.

As such, we have found that it is much easier to work in terms of time domain variables. That is, the CFD solution and CFD residual stored at N_T discrete and equally spaced "subtime" levels over the period T ($T = 2\pi/\omega$) of a single cycle of unsteadiness. We begin by setting

$$\boldsymbol{\mathcal{Q}}_{l,j} = \left\{ \begin{array}{c} Q_{l,j}(t_0 + \Delta t) \\ Q_{l,j}(t_0 + 2\Delta t) \\ \\ \vdots \\ \\ Q_{l,j}(t_0 + T) \end{array} \right\} \tag{35}$$

and

$$\boldsymbol{\mathcal{N}}_{l,j} = \left\{ \begin{array}{c} N_{l,j}(t_0 + \Delta t) \\ N_{l,j}(t_0 + 2\Delta t) \\ \\ \vdots \\ \\ N_{l,j}(t_0 + T) \end{array} \right\} \tag{36}$$

where $\Delta t = 2\pi/N_T\omega$. One can then relate $\hat{\boldsymbol{\mathcal{Q}}}_{l,j}$ to $\boldsymbol{\mathcal{Q}}_{l,j}$, and $\hat{\boldsymbol{\mathcal{N}}}_{l,j}$ to $\boldsymbol{\mathcal{N}}_{l,j}$, via a constant $N_T \times N_T$ Fourier transform matrix $\mathbf{E}$. i.e.

$$\hat{\boldsymbol{\mathcal{Q}}}_{l,j} = \mathbf{E}\boldsymbol{\mathcal{Q}}_{l,j} \qquad \text{and} \qquad \hat{\boldsymbol{\mathcal{N}}}_{l,j} = \mathbf{E}\boldsymbol{\mathcal{N}}_{l,j} \tag{37}$$

where

$$\mathbf{E} = \frac{1}{N_T} \begin{bmatrix} \cos\left(2\pi\frac{0\times1}{N_T}\right) & \cos\left(2\pi\frac{0\times2}{N_T}\right) & \cdots & \cos\left(2\pi\frac{0\times N_T}{N_T}\right) \\ \cos\left(2\pi\frac{1\times1}{N_T}\right) & \cos\left(2\pi\frac{1\times2}{N_T}\right) & \cdots & \cos\left(2\pi\frac{1\times N_T}{N_T}\right) \\ & \vdots & & \\ \cos\left(2\pi\frac{N_H\times1}{N_T}\right) & \cos\left(2\pi\frac{N_H\times2}{N_T}\right) & \cdots & \cos\left(2\pi\frac{N_H\times N_T}{N_T}\right) \\ \sin\left(2\pi\frac{1\times1}{N_T}\right) & \sin\left(2\pi\frac{1\times2}{N_T}\right) & \cdots & \sin\left(2\pi\frac{1\times N_T}{N_T}\right) \\ & \vdots & & \\ \sin\left(2\pi\frac{N_H\times1}{N_T}\right) & \sin\left(2\pi\frac{N_H\times2}{N_T}\right) & \cdots & \sin\left(2\pi\frac{N_H\times N_T}{N_T}\right) \end{bmatrix} \tag{38}$$

Thus Eq. 32 can be rewritten as

$$\omega\mathbf{A}\mathbf{E}\boldsymbol{\mathcal{Q}}_{l,j} + \mathbf{E}\boldsymbol{\mathcal{N}}_{l,j} = \hat{\mathbf{0}} \tag{39}$$

and subsequently multiplying this equation by the inverse of $\mathbf{E}$ results in

$$\omega\mathbf{E}^{-1}\mathbf{A}\mathbf{E}\boldsymbol{\mathcal{Q}}_{l,j} + \mathbf{E}^{-1}\mathbf{E}\boldsymbol{\mathcal{N}}_{l,j} = \hat{\mathbf{0}} \tag{40}$$

or equivalently

$$\omega\mathbf{D}\boldsymbol{\mathcal{Q}}_{l,j} + \boldsymbol{\mathcal{N}}_{l,j} = \hat{\mathbf{0}} \tag{41}$$

where $\mathbf{D} = \mathbf{E}^{-1}\mathbf{A}\mathbf{E}$. One can then pseudo time march Eq. 41 to solve for the solution $\boldsymbol{\mathcal{Q}}_{l,j}$. i.e. march the equation

$$\frac{\delta\boldsymbol{\mathcal{Q}}_{l,j}}{\delta t} + \omega\mathbf{D}\boldsymbol{\mathcal{Q}}_{l,j} + \boldsymbol{\mathcal{N}}_{l,j} = \hat{\mathbf{0}} \tag{42}$$

where for example, if one were using an explicit time marching technique for their nominal CFD method, they could iterate the following equation to obtain the HB solution

$$\boldsymbol{\mathcal{Q}}^{n+1}_{l,j} = \boldsymbol{\mathcal{Q}}^{n}_{l,j} - \Delta t_{l,j}(\omega\mathbf{D}\boldsymbol{\mathcal{Q}}^{n}_{l,j} + \boldsymbol{\mathcal{N}}^{n}_{l,j}). \tag{43}$$

Implementing the HB method (Eq. 41) within an existing flow solver is easy to do. All that is required is a redimensioning of the primary arrays by a factor of N_T and the implementation of a "do-loop" about the residual computation section of code.. If the nominal flow solver can be expressed in pseudo code as

```
DO
   CALL RESIDUAL(Q(:),X(:),DQ(:))
   Q(:) = Q(:) + DQ(:)
   CALL CHECK_CONVERGENCE(DQ(:),L2_RESIDUAL)
   IF (L2_RESIDUAL < CONVERGENCE_TOLERANCE) EXIT
ENDDO
```

then the HB/CFD variant of that same solver can be written as

```
DO
   DO N = 1,2*N_HARMONICS+1
      CALL RESIDUAL(QHB(N,:),XHB(N,:),DQHB(N,:))
   ENDDO
   CALL SOURCE_HB(QHB(:,:),SOURCE_TERM_HB(:,:))
   QHB(:,:) = QHB(:,:) + DQHB(:,:) + SOURCE_TERM_HB(:,:)
   CALL CHECK_CONVERGENCE_HB(DQHB(:,:),L2_RESIDUAL)
   IF (L2_RESIDUAL < CONVERGENCE_TOLERANCE) EXIT
ENDDO
```

where `QHB(:,:)` and `DQHB(:,:)` are harmonic balance solver arrays, which are similar to the arrays `Q(:)` and `DQ(:)` that store the CFD solution and CFD solution residual in the nominal code, yet these arrays have an extra dimension of N_T in order to store each HB solution and solution residual at the N_T subtime levels over a time period of unsteadiness. The array `SOURCE_TERM_HB(:,:)` represents the term $\omega\mathbf{D}\boldsymbol{\mathcal{Q}}_{l,j}$ in Eq. 41.

Note, two other minor modifications have to be made to the nominal CFD solver code in order to implement the HB method. One is to add the necessary code to treat the effect of unsteady CFD mesh motion, and the other is the code to handle the unsteady solid wall boundary conditions. For the mesh motion effect, one simply modifies the flux computation routines where for instance, if $F_{l,j}$ represents the l^{th} element of the x component flux at mesh point j, $F_{l,j}$ would be modified to be

$$F_{l,j}(t_n) = F_{l,j}(t_n) - \dot{x}(t_n)\, Q_{l,j}(t_n) \tag{44}$$

in the HB solver. If we let $\boldsymbol{\mathcal{X}}_j$ be a vector whose elements are the x component of mesh point j at the

N_T subtime levels over a period of oscillation, i.e.,

$$\boldsymbol{\mathcal{X}}_j = \left\{ \begin{array}{c} x_j(t_0 + \Delta t) \\ x_j(t_0 + 2\Delta t) \\ \\ \vdots \\ \\ x_j(t_0 + T) \end{array} \right\}, \tag{45}$$

and if we let $\dot{\boldsymbol{\mathcal{X}}}_j$ be a vector whose elements are the time derivative of the x component of mesh point j at the NT subtime levels over a period of oscillation, i.e. $\dot{x}(t_n)$,

$$\dot{\boldsymbol{\mathcal{X}}}_j = \left\{ \begin{array}{c} \dot{x}_j(t_0 + \Delta t) \\ \dot{x}_j(t_0 + 2\Delta t) \\ \\ \vdots \\ \\ \dot{x}_j(t_0 + T) \end{array} \right\}, \tag{46}$$

it can be shown that $\dot{\boldsymbol{\mathcal{X}}}_j$ is related to $\boldsymbol{\mathcal{X}}_j$ via the following equation

$$\dot{\boldsymbol{\mathcal{X}}}_j = \omega \mathbf{D} \boldsymbol{\mathcal{X}}_j \tag{47}$$

The vector $\dot{\boldsymbol{\mathcal{X}}}_j$ can be determined before the HB solution process begins. The y and z flux components are modified in a similar manner. i.e.

$$G_{l,j}(t_n) = G_{l,j}(t_n) - \dot{y}(t_n)\, Q_{l,j}(t_n) \tag{48}$$

$$H_{l,j}(t_n) = H_{l,j}(t_n) - \dot{z}(t_n)\, Q_{l,j}(t_n) \tag{49}$$

Next, in order to represent viscous solid wall boundary conditions with the HB method, all that is necessary is to modify the subroutine that treats the solid wall boundary conditions such that the velocity components at the wall are set to

$$u_j(t_n) = \dot{x}(t_n) \qquad v_j(t_n) = \dot{y}(t_n) \qquad w_j(t_n) = \dot{z}(t_n). \tag{50}$$

Results

Experimental Data

Figure 1 shows forward wingtip launcher accelerometer LCO response level versus Mach number for 2000 feet altitude flight tests where the F-16 was carrying the following arrangement of weapons and external stores: Station 1 (wingtip) - LAU-129/A Launcher, Station 2 (under-wing - y=157in) - LAU-129 Launcher with AIM-9P Missile, Station 3 (underwing - y=120in) Launcher/Pylon with Air-Ground Missile, and Station 4 (underwing - y=71in) Fuel Tank Pylon with Empty 370 Gallon Fuel Tank. The F-16 is a Block 40 F-16C modified for flutter testing, tail number 88-0441[7]

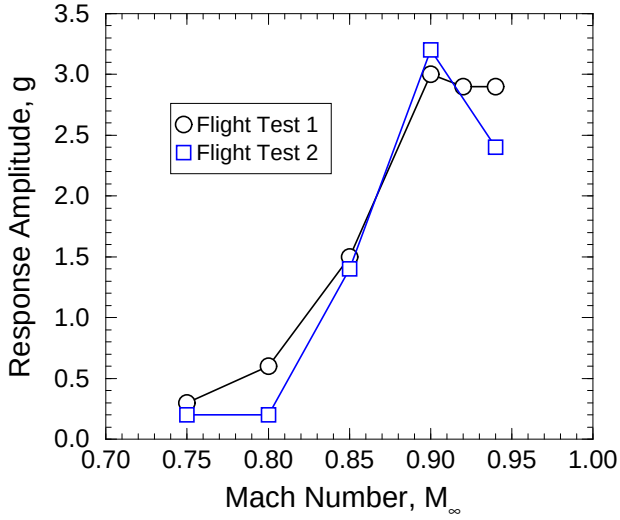

Fig. 1 Experimental F-16 Forward Wingtip Launcher Accelerometer LCO Response Level Versus Mach Number for an Altitude of 2000 feet.

Computational Model

Structural Model

The structural portion of the aeroelastic model consists of modal masses and mode shapes obtain from a NASTRAN finite-element model. Only antisymmetric modes are used since flutter onset and LCO are antisymmetric as has been previously demonstrated in experiment and computational studies by the present authors and others. Figure 2 shows the first two antisymmetric mode shapes. The mode shapes have been fit to the CFD grid using a sixth-order least squares polynomial fitting technique.

Fluid Dynamic Model

Only the F-16 wing is modeled in the present CFD analysis. The effects of the fuselage, horizontal tail, vertical tail, external weapons and stores as such are not modeled aerodynamically. However, their structural inertia and stiffness are included in the structural part of the overall aeroelastic analysis. Later in the paper, we will extend the wingtip by six inches in an effort to account for the aerodynamic effect of the wingtip launchers. We have found the flutter onset Mach number to be sensitive to the geometry of the F-16 wingtip. We currently do not have the capability in our CFD solver to model the detailed geometry of the wingtip launcher.

The CFD method used in the present analysis is a variant of the standard Lax-Wendroff scheme[8–10] in conjunction with the one-equation turbulence model of Spalart and Allmaras.[11] As also reported in Ref. [1], shown in Fig. 3 is the computational grid for the F-16 wing surface (Fig. 3a) and wing symmetry plane (Fig. 3b). The mesh uses 65 (mesh i coordinate) computational nodes about the wing in the stream-wise direction, 33 (mesh j coordinate) nodes normal to the

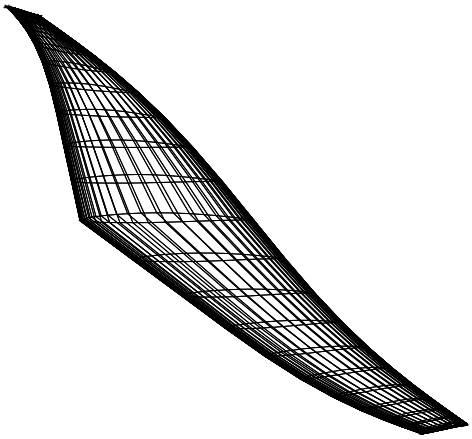

a) Mode 2 - 8.168 Hz

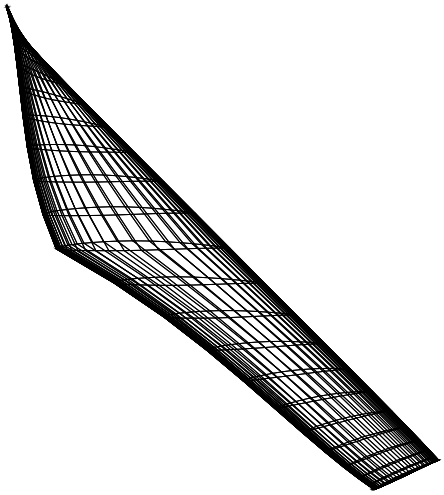

b) Mode 4 - 8.672 Hz

Fig. 2 F-16 First Two Anti-Symmetric Structural Modes.

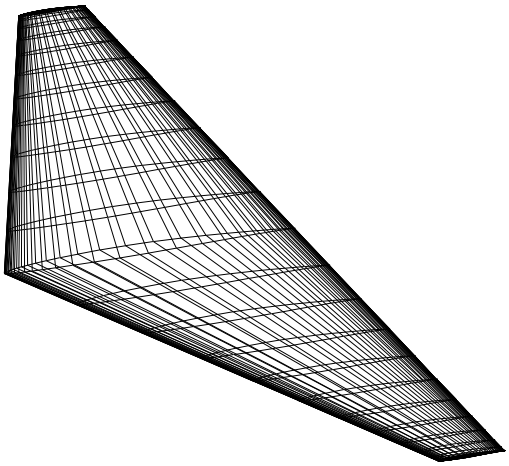

a) Wing Surface Grid

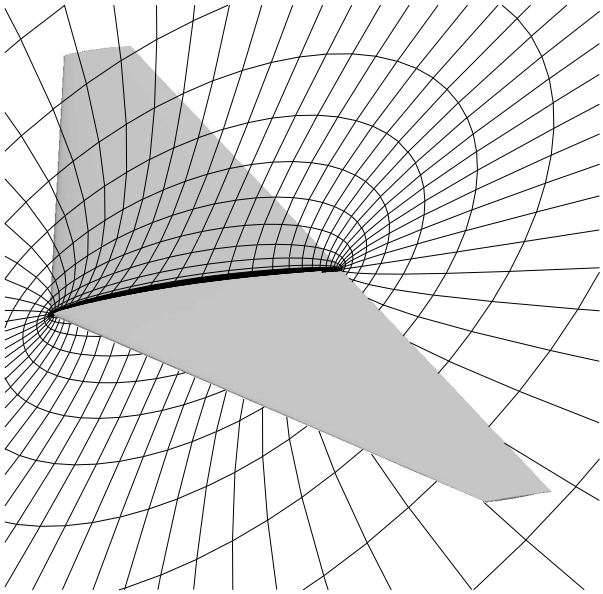

b) Wing Symmetry Plane Grid

Fig. 3 F-16 Wing Computational Grid.

wing, and 25 (mesh k coordinate) nodes along the span, with 12 more nodes wrapping around each wing tip for a total of 49 mesh points in the span-wise direction. The outer boundary of the grid extends ten wing semi-spans from the mid-chord of the wing at the symmetry plane. Grid spacing near the surface is close enough to ensure that $y+$ distances (a measure boundary layer grid resolution) are always less than 10 over the entire wing, and for most of the wing, less than five.

Figure 4 shows computed viscous steady flow surface pressure contours (Fig. 4a) and Mach number contours in the wing symmetry plane (Fig. 4b) for a freestream Mach number of $M_\infty = 0.9$, steady angle-of-attack of $\bar{\alpha}_0 = 1.5$ degrees, and sea level altitude. Standard atmosphere conditions are assumed. For this Mach number and altitude, the Reynolds number based on the wing root chord is $Re_{\infty_{c_r}} = 104 \times 10^6$.

For the analysis presented in this paper, we consider straight and level flight, and as an initial approximation, we consider the angle-of-attack of $\bar{\alpha}_0 = 1.5$ degrees to be constant over the range of transonic Mach numbers considered. Experimental data shows that the mean angle-of-attack $\bar{\alpha}_0$ varies only by a fraction of a degree in the transonic Mach number range.

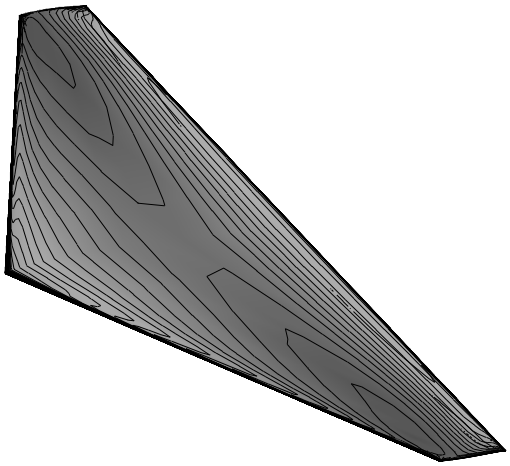

a) Surface Pressure Contours

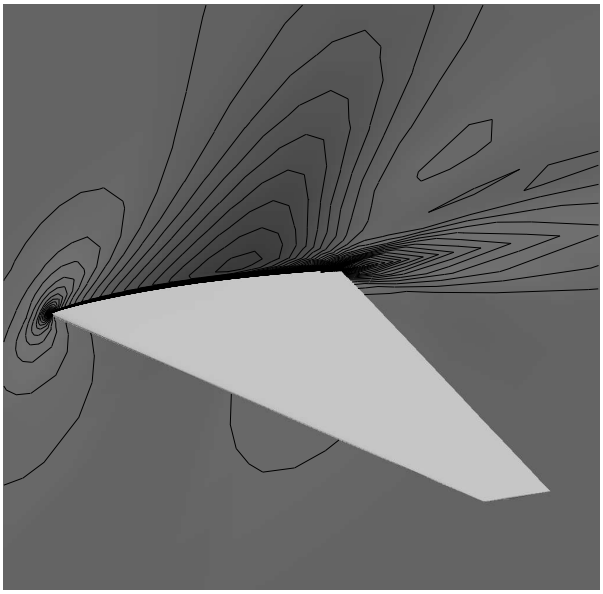

b) Wing Symmetry Mach Number Contours

Fig. 4 F-16 Steady Flow Pressure and Mach Number Contours, $M_\infty = 0.9$, $\bar{\alpha}_0 = 1.5$ deg., Sea Level Altitude ($h = 0$ feet), $Re_{\infty_{c_r}} = 104 \times 10^6$.

Flutter Onset

Structural Modal Refinement

We first want to make sure we are using a sufficient number of structural modes in the aeroelastic model. Table 1 shows the trend for flutter onset Mach number at 2000 and 10000 feet. As can be seen, just using the first two mode shapes provides a very well converged solution for the flutter onset Mach number for both altitudes. We take advantage of this in the remainder of the paper. Using only two structural modes helps to decrease the computational time required. The cost of the HB/LCO method is proportional the number of structural modes used. Note, the generalized masses for the first two structural modes used in the present calculations are $\mathcal{M}_{2,2} = 1.576$ and $\mathcal{M}_{4,4} = 0.6723$ rather than $\mathcal{M}_{2,2} = 1.000$ and $\mathcal{M}_{4,4} = 1.000$ as employed in Ref. [1]. The units of mass are $lbf \times in/sec^2$.

Structural Modes	Altitude (feet) 2000	10000
2	-	-
2,4	0.9012	1.096
2,4,6	0.9018	1.098
2,4,6,8	0.9042	1.108
2,4,6,8,10	0.9064	1.115
2,4,6,8,10 and Rigid Roll	0.8994	1.103

Table 1 Sensitivity of Computed Flutter Onset Mach Number to the Number of Structural Modes Used in HB/LCO Model for 2000 and 10000 feet, $\bar{\alpha}_0 = 1.5$ deg.

LCO

Shown in Fig. 5 is the gravitational "g-level" response of the forward end of the wingtip launcher as a function of Mach number at a 2000 feet altitude when considering a number of different parameters related to the elements of the aeroelastic computational model. Namely:

1. Mean Angle-of-Attack.
2. Effect of Modifying Wing Geometry to Account of Wingtip Launcher.
3. Precise Wing Twist Definition.
4. Static Aeroelastic Deformation Effects.

One additional feature that we would like to be able to model is the gravitational effect. However unfortunately at the present time, we do not have the knowledge of the wing mass distribution which is necessary in order to do this.

Mean Angle of Attack Sensitivities

The LCO curves which bend over significantly in Fig. 5 correspond to the straight untwisted wing. As can be seen, the LCO response behavior is strongly nonlinear in this case. Also, the flutter onset Mach number can be seen to decrease with increasing wing mean angle-of-attack. The change in Mach number is significant considering that only a one degree change in overall angle-of-attack is considered. However, the maximum LCO response level remains relatively constant and similar to that observed in flight test.

Wing Tip Geometry

As can be seen in Fig. 5, for the nominal wing geometry and untwisted wing model, the flutter onset and

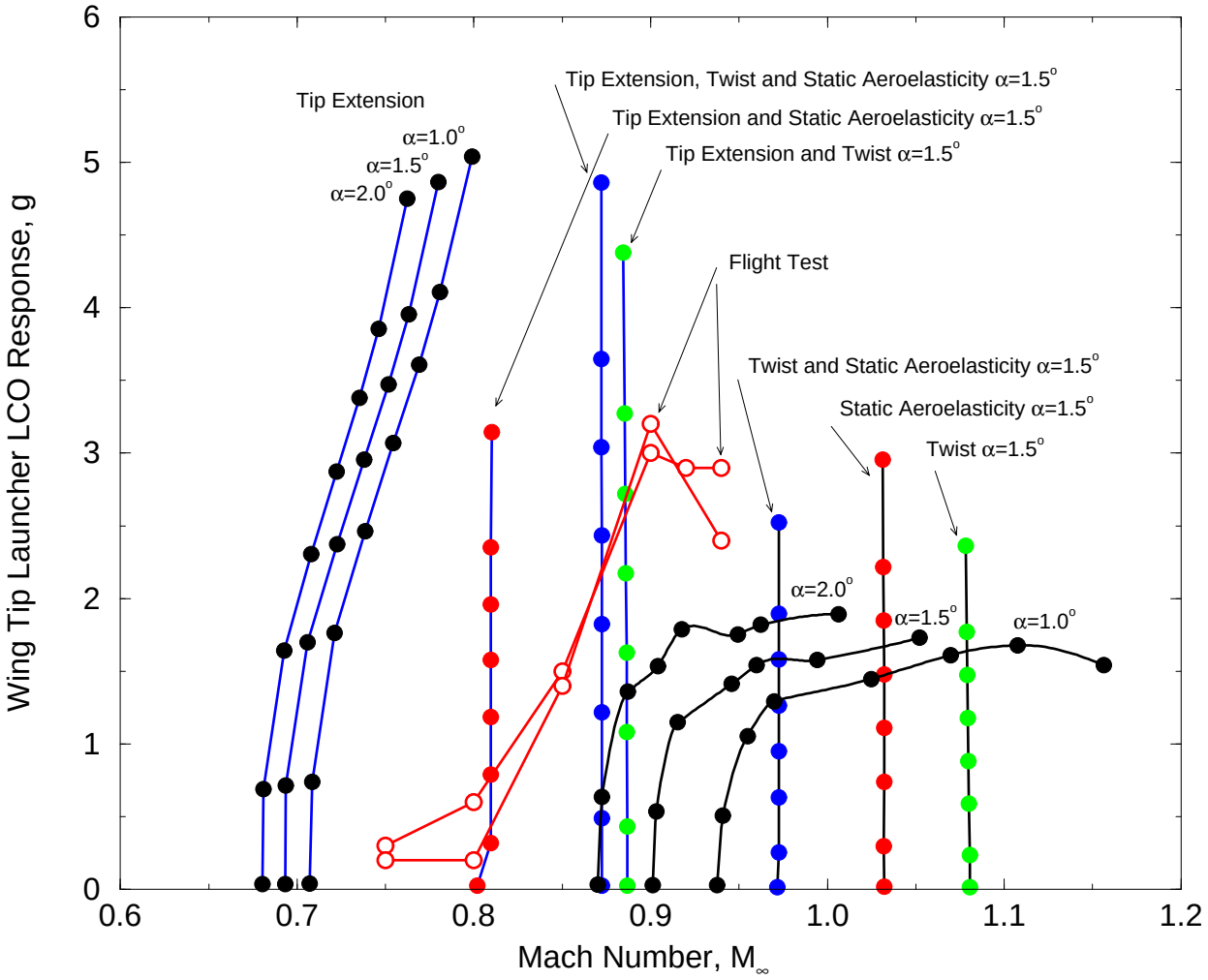

Fig. 5 Computed LCO Response at the Location of the Forward Wingtip Launcher, 2000 feet.

LCO response curves are a bit high in Mach number when compared to flight test results. Denegri (private communication) has observed when using double lattice flutter calculations that modeling the wingtip launchers is very important. The flutter onset velocity is significantly less (30% or more) when modeling the wingtip launcher even when the launcher is modeled as a simple flat plate strip in the double lattice code. Therefore, and as an initial crude approximation, we have elected to study the sensitivity of flutter onset and LCO behavior when slightly extending the span of the wing at the wingtip, in this case, by six inches. The actual wingtip launcher has a width of about eight inches. As can be seen in Fig. 5, this simple modification results in a significant reduction of flutter onset and LCO Mach number. The LCO curves are also much steeper indicating that the LCO behavior is less nonlinear, which is most likely due to the lower Mach numbers. Currently, we are studying the feasibility of modifying our model to include a slender body representation of tip store aerodynamics.

Precise Wing Twist Definition

Data on the precise wing twist definition has been recently provided to us. Figure 6 shows the airfoil section at the wingtip. As can been, the level of twist is significant. The twist definition is confidential, so we cannot state it here. Figure 5 shows the flutter onset and LCO response, for $\alpha_0 = 1.5$ degrees, and for both the nominal wing shape and nominal wing shape with tip extension, in the case of the model using the precise wing twist. As can be seen, the flutter Mach number increases, and the LCO behavior is changed substantially when including the wing twist for both wing geometries. This has led us to also consider static aeroelastic deformation effects.

Static Aeroelastic Deformation Effects

We next consider the addition of static aeroelastic effects for both wing geometries and for both wing twist and no wing twist test cases. Figure 6 shows, for the nominal wing shape, the airfoil section at the wingtip when including static aeroelastic effects at the flutter onset point. As can be seen, including static aeroelastic effects further increases the nose down twist

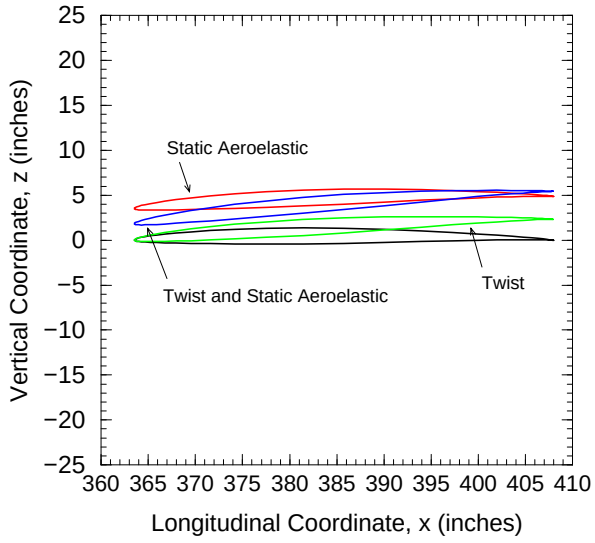

a) True Scale

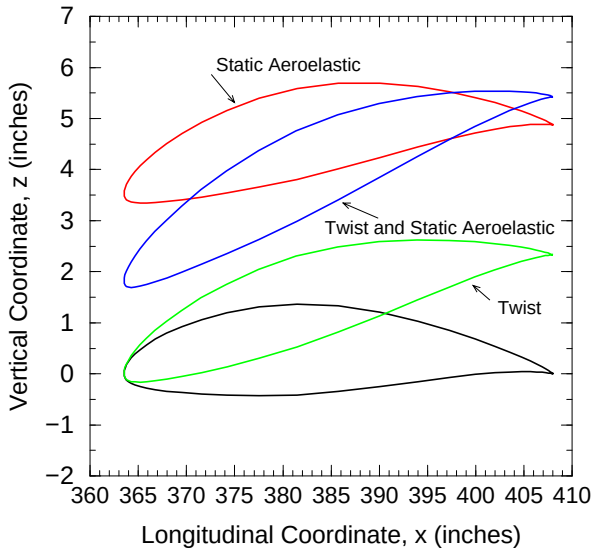

b) Distorted

Fig. 6 Wingtip Airfoil Section Profiles

effect, thus further adding to overall nose down twist at the wingtip.

Figure 5 shows the LCO response for $\alpha_0 = 1.5$ degrees, for both the nominal wing shape and nominal wing shape with tip extension, and for the wing with twist and no twist, when also including static aeroelastic effects. As can be seen, the flutter onset Mach number increases, and the LCO behavior is significantly changed when including the static aeroelastic effect for both wing geometries.

Gravitational Effects

The remaining effect that we have not yet been able to include is the gravitational effect. As mentioned previously, unfortunately we do not at the present time have information about the mass distribution of the wing needed in order to account for this effect. Our thoughts are that perhaps adding in this effect to the model will further modify the flutter onset and LCO behavior, whereby we may again predict strong nonlinear LCO behavior with the gravity loading counteracting the effect of wing twist and static aeroelastic deformation.

Conclusions

The computation of the limit cycle oscillation behavior of the F-16 fighter using a nonlinear frequency domain harmonic balance is demonstrated. In this latest effort, we consider the sensitivity of the model to various parameters such as mean angle-of-attack, wingtip geometry, wing twist, and static aeroelastic deformation. Further refinements of the model appear to be required, especially in modeling the precise geometry of the wingtip in case of where the wing has a wingtip missile launcher.

Acknowledgments

This work is being supported by AFOSR grant, "Theoretical Predictions of Limit Cycle Oscillations for Flight Flutter Testing". The program manager is Dr. Neal Glassman and the key technical point of contact in the SEEK EAGLE office at Eglin AFB is Dr. Charles Denegri.

References

[1]Thomas, J. P., Dowell, E. H., and Hall, K. C., "Modeling Limit Cycle Oscillation Behavior of the F-16 Fighter Using a Harmonic Balance Approach," AIAA Paper 2004-1696, Presented at the 45th AIAA/ASME/ASCE/AHS/ASC Structures, Structural Dynamics and Materials (SDM) Conference, Palm Springs, CA.

[2]Hall, K. C., Thomas, J. P., and Clark, W. S., "Computation of Unsteady Nonlinear Flows in Cascades Using a Harmonic Balance Technique," *AIAA Journal*, Vol. 40, No. 5, May 2002, pp. 879–886.

[3]Thomas, J. P., Dowell, E. H., and Hall, K. C., "Nonlinear Inviscid Aerodynamic Effects on Transonic Divergence, Flutter and Limit Cycle Oscillations," *AIAA Journal*, Vol. 40, No. 4, April 2002, pp. 638–646.

[4]Thomas, J. P., Dowell, E. H., and Hall, K. C., "Modeling Viscous Transonic Limit Cycle Oscillation Behavior Using a Harmonic Balance Approach," AIAA Paper 2002-1414.

[5]Thomas, J. P., Dowell, E. H., and Hall, K. C., "A Harmonic Balance Approach for Modeling Three-Dimensional Nonlinear Unsteady Aerodynamics and Aeroelasticity," ASME Paper IMECE-2002-32532.

[6]Thomas, J. P., Hall, K. C., and Dowell, E. H., "A Harmonic Balance Approach for Modeling Nonlinear Aeroelastic Behavior of Wings in Transonic Viscous Flow," AIAA Paper 2003-1924.

[7]Charles M. Denegri, J. and Dubben, J. A., "In-Flight Wing Deformation Characteristics During Limit Cycle Oscillations," AIAA Paper 2003-1426.

[8]Ni, R.-H., "A Multiple Grid Scheme for Solving the Euler Equations," *AIAA Journal*, Vol. 20, No. 11, November 1982, pp. 1565–1571.

[9]Davis, R. L., Ni, R. H., and Bowley, W. W., "Prediction of Compressible, Laminar Viscous Flows Using a Time-Marching Control Volume and Multiple-Grid Technique," *AIAA Journal*, Vol. 22, No. 11, November 1984, pp. 1573–1581.

[10]Saxor, A. P., "A Numerical Analysis of 3-D Inviscid Stator/Rotor Interactions Using Non-Reflecting Boundary Conditions," Tech. Rep. 209, MIT, March 1992, Gas Turbine Laboratory Report 209.

[11]Spalart, P. R. and Allmaras, S. R., "A One Equation Turbulence Model for Aerodynamic Flows," AIAA Paper 92–0439.